

Mass and wind axial angular-momentum responses to mountain torques in the 1–25 day band: Links with the Arctic Oscillation

By FRANÇOIS LOTT* and FABIO D'ANDREA
LMD/IPSL Ecole Normale Supérieure, Paris

(Received 27 August 2003; revised 27 September 2004)

SUMMARY

Using the NCAR/NCEP reanalysis data, we analyse the atmospheric angular momentum M response to torques T in the 1–25 d spectral band. At these periodicities, the variations in M are equally distributed between variations in wind angular momentum M_R and mass angular momentum M_Ω . They are driven by mountain torques T_M which are substantially larger than boundary-layer torques T_B . This equipartition between M_R and M_Ω occurs because the response to T_M in most cases satisfies the geostrophic balance, and because the major mountain ranges are located in the midlatitudes. At these latitudes, an external positive zonal-mean zonal force is in good part equilibrated by a flux of mass equatorward through the Coriolis force, a process that increases M_Ω . In geostrophic balance with this mass redistribution, the zonal-mean zonal wind increases where the force is applied and M_R increases as well. This process leads to $M_R \approx M_\Omega$ for parameters representative of the earth's atmosphere.

This explanation of the equipartition between M_Ω and M_R is confirmed by two pieces of independent evidence. The first is based on the reanalysis data, in which we evaluate the contribution of six non-overlapping latitudinal sectors to T_M hence varying the importance of the Coriolis force. When the mountain torque T_M is produced by mountains located in the Arctic and Antarctic sectors, the changes in M_Ω dominate those in M_R . It is the other way round when T_M is produced by mountains located in the equatorial sector and $M_\Omega \approx M_R$ when T_M is due to mountains located in the subtropics or in the midlatitudes.

The second is based on results from a one-layer shallow-water axisymmetric model on a sphere, where zonal body forces centred at different latitudes are specified. The latitudinal dependence of the repartition between M_R and M_Ω found in the data is reproduced by the model with $M_\Omega \approx M_R$ when the force is centred in the midlatitudes.

The Arctic Oscillation (AO) pattern being associated with substantial M_Ω , the significance of these results for the atmospheric circulation variability is also discussed. In the 1–25 d band, the AO variations are very significantly related to M_Ω variations driven by T_M . This result suggests that in this band the mountain ranges substantially affect the AO variability.

KEYWORDS: Atmospheric angular momentum budget Geostrophic adjustment

1. INTRODUCTION

Variations of the atmospheric axial angular momentum (AAM, or M in equations) are known to occur at time-scales from daily to interannual (Rosen and Salstein 1983). In fact, they are associated with dynamical processes having different characteristic time-scales, such as the El Niño Southern oscillation (Wolf and Smith 1987; Chao 1984), the 40–60 d intraseasonal tropical oscillation (Madden 1987), and the 15–35 d intraseasonal midlatitudes oscillations (Lott *et al.* 2004). At smaller periodicities they are also associated with travelling Rossby waves (Lejenäs and Madden 2000) and synoptic-scale midlatitude systems (Iskenderian and Salstein 1998).

The exchange of angular momentum with solid earth is achieved by the friction torque T_B and the mountain torque T_M (Starr 1948) whose relative importance depends on the time-scale. The mountain torque is generally weaker than the friction torque on interannual and seasonal time-scales (Newtown 1971) with the possible exception of periods of El Niño events (Wolf and Smith 1987). The friction torque also seems to produce the AAM changes that occur during the intraseasonal tropical oscillation (Madden 1987). Nevertheless, there are examples of intraseasonal tropical oscillations during northern hemisphere winter where the mountain torque drives substantially the AAM changes while the friction torque damps them (Weickmann and Sardeshmuckh

* Corresponding author: Laboratoire de Météorologie Dynamique du CNRS, Ecole Normale Supérieure, 24, rue Lhomond, 75231 PARIS cedex 05, France. e-mail: flott@lmd.ens.fr

1994; Weickmann *et al.* 1997). This fact becomes even more valid as the time-scale decreases below the intraseasonal tropical oscillations periodicities of 40–60 d (Dickey *et al.* 1991; Lott *et al.* 2001). At even smaller periods the mountain torque clearly drives the changes in AAM (Swinbank 1985; Iskenderian and Salstein 1998). These results are in agreement with Rosen's (1993) conclusion that the friction torque dominates the changes in AAM on time-scales of months, whereas on time-scales shorter than several weeks the mountain torque is dominant.

Although the relative importance of mountain torques and friction torques in producing the AAM changes has been often discussed, there are comparatively few studies that document the relative importance of the mass angular momentum M_Ω and of the wind angular momentum M_R for the AAM itself. This is due to the fact that M_Ω makes a rather small contribution to M , the changes in M_Ω being only comparable to those in M_R at periodicities $\omega^{-1} < 25$ d (Lott *et al.* 2004), ω being the frequency in cycles per day. At larger periodicities the spectra of the M_R tendency is much larger than that of the M_Ω tendency. In this case the tropical regions largely control the AAM changes through the Pacific Ocean friction torques associated with convective fluctuations over the Indo-Pacific warm pool (Madden 1987; Hendon 1995).

The equipartition between M_R and M_Ω can have a simple dynamical origin. When a positive torque T_M is due to a mountain range located in the extratropics, providing we can neglect its effect over long distances through travelling Rossby waves, it accelerates the zonal-mean flow in the extratropics. The positive barotropic zonal wind this torque produces (producing positive M_R) is affected by the geostrophic balance. Thus, this torque also induces changes of zonal-mean mass to the north and to the south of the central latitude of the mountain range (producing M_Ω). Hence this torque naturally affects both M_Ω and M_R but in a fraction that remains to be evaluated. Note as well that this fraction has to vary with the latitude of the mountains that produce T_M , because the Coriolis parameter and the distance to the earth axis vary with latitude.

It is important to emphasize that analysing the response in M_Ω to mountain torques is not only relevant to understanding the AAM budget closure at high frequencies. It is also interesting in addressing the role of mountains on the general circulation of the atmosphere. Indeed, there are increasing evidences that AAM budget studies can help to isolate to which extent the atmospheric variability in the midlatitudes is driven by mountains (Lott *et al.* 2004). In this context, Lott *et al.* (2004) found that changes in the Arctic Oscillation (Wallace 2000) in the 20–30 d band are preceded by a small but significant signal in the mountain torque. This relationship is mainly due to the fact that the Arctic Oscillation pattern corresponds to a redistribution of mass from the polar latitudes to the midlatitudes, hence giving a substantial contribution to M_Ω . These findings are supported by von Storch (1994, 1999) who found in a coupled general-circulation model (GCM) that two among the three dominant modes of large-scale variability are associated with larger M_Ω than M_R . For completeness, note as well that Kang and Lau (1994) related the principal modes of atmospheric circulation variability to AAM fluctuations but limited their analysis to changes in M_R .

The first purpose of the present study is to analyse the repartition between mass and wind angular momentum due to mountain torques at periodicities for which the friction torque makes a small contribution to the AAM budget. The second purpose is to interpret this repartition as a natural consequence of the geostrophic equilibrium that takes place in the midlatitude, that is at the latitudes where the mountains mainly affect the zonal-mean flow. The third is to suggest, using different diagnostics than in Lott *et al.* (2004), that mountain torques drive in part the changes in the Arctic Oscillation that occur at periodicities $\omega^{-1} < 25$ d, because they modify the mass angular momentum.

In section 2, we present the data used and recall briefly some spectral analysis results that motivate the present work. In section 3, we focus on the AAM budget in the 1–25 d band and look at the real atmosphere response to torques due to mountains located in different latitude bands. In section 4, we analyse the geostrophic adjustment to mountain torques using a zonally averaged barotropic shallow-water model on the sphere. Section 5 gives some conclusion.

2. DATA DESCRIPTION

(a) AAM budget and AO

We use 40 years (1958–97) of the NCEP/NCAR* reanalysis (Kalnay *et al.* 1996) to extract the daily averages of the surface pressure field P_s , the sea-level pressure field P_m , the zonal wind u at the 17 pressure levels given by the analysis, and the daily average of the boundary-layer stress τ_B issued from 6-hour forecasts. From this set of data we evaluate the global tendency budget of the atmospheric angular momentum M :

$$\frac{dM}{dt} = \frac{d(M_R + M_\Omega)}{dt} = T_M + T_B, \quad (1)$$

where M_R , M_Ω , T_M , and T_B are the wind angular momentum, the mass angular momentum, the torque due to the mountains, and the torque due to the boundary-layer stress, respectively. These four quantities are computed as

$$M_R = \int_V \rho r \cos \theta u \, dV, \quad M_\Omega = \int_V \rho \Omega r^2 \cos^2 \theta \, dV, \quad (2)$$

$$T_M = - \int_S P_s \frac{\partial Z_s}{\partial \lambda} \, dS, \quad T_B = \int_S r \cos \theta \tau_B \, dS. \quad (3)$$

In Eqs. (2)–(3), $\int_V dV$ is the integral over the volume atmosphere, $\int_S dS$ is the integral over the earth surface, ρ is the density, λ is the longitude, θ is the latitude, r is the radius of the earth, Ω is the angular velocity of earth's rotation, and Z_s is the topographic height.

In our calculation the AAM budget is well balanced: the correlation between $d(M_R + M_\Omega)/dt$ and $T_M + T_B$ in Eq. (1) is close to 0.85 (Lott *et al.* 2004). Note that the contribution of the NCEP model's parametrized mountain gravity-wave drag was not included in the mountain torque, because it degrades the balance between the global AAM tendency and the torques (Huang *et al.* 1999).

The dominant large-scale atmospheric pattern that accompanies changes in M_Ω is displayed in Fig. 1(a). To reduce the influence of the annual cycle and to focus on the northern hemisphere, it is computed as winter (December to February, hereafter DJF) regression of the sea-surface-pressure field onto M_Ω (Von Storch and Zwiers 1999). Figure 1(a) shows that the northern hemisphere changes associated with positive M_Ω are first due to a redistribution of mass from the polar latitudes to the midlatitude ones. The geostrophic balance implies that they are associated with changes in the midlatitude and polar jet, with a reinforced jet over the north-east and central Pacific as well as over the central eastern North Atlantic.

From this set of data, we also compute the Empirical Orthogonal Functions (EOFs) (Preisendorfer 1988) of the sea-surface-pressure P_m daily variability over the northern

* National Centers for Environmental Prediction/National Center for Atmospheric Research.

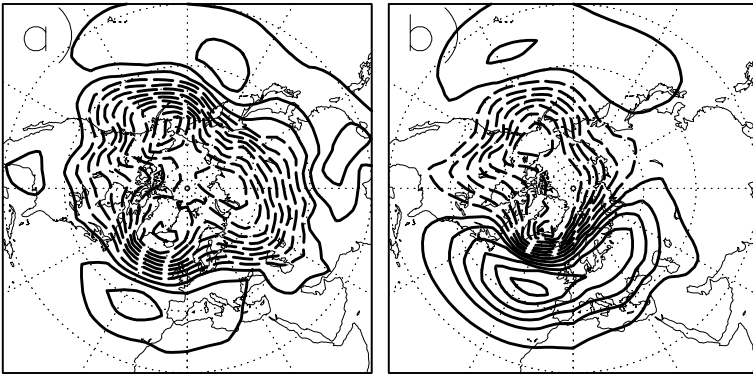


Figure 1. Winter (DJF) regression of sea-level-pressure maps P_m on (a) the mass angular momentum M_Ω (contour interval 0.5 hPa) and (b) the Arctic Oscillation index, or first principal component of DJF P_m daily variability (contour interval 1 hPa). Negative contours are dashed.

hemisphere and during winter months. The first EOF (EOF 1) accounts for 9.3% of the daily DJF variability. The DJF regression of the sea-level pressure P_m onto its first principal component (PC 1), shown in Fig. 1(b), is strongly reminiscent of the Arctic Oscillation (Thomson and Wallace 1998): it is strongly zonally symmetric and associated with reinforced jets over the north-east and central Pacific, as well as over the central eastern North Atlantic. Consequently, the Arctic Oscillation index used in the rest of this paper will be the P_m PC 1. It is important to emphasize here that the two maps in Fig. 1(a) and Fig. 1(b) have a pattern correlation above 0.6, when evaluated north of 30°N . This good correlation is at the basis of the lead-lag relationships between mountain torque, mass AAM and the AO in the 20–30 d band, found in Lott *et al.* (2004).

(b) Spectral analysis

To illustrate the relevance of the high-pass $\omega^{-1} < 25$ d window, Fig. 2 presents the spectra of each term in the AAM budget (Eqs. (1)–(3)), as well as the coherency between the global AAM M and both torques T_M and T_B . To highlight high-frequency contributions, the spectra in Figs. 2(a)–(b) are presented in the linear-log energy-conserving representation. Both the spectra of the M_R tendency and the spectra of the M_Ω tendency present a flat background of nearly equal intensity for $\omega^{-1} < 20$ d. At longer periodicities, the contribution of M_R exceeds that of M_Ω , with the latter becoming less than half the former for $\omega^{-1} > 25$ d. For the torques, the spectra in Fig. 2(b) show that at periodicities typically above 30–40 d, the contributions of T_M and T_B are comparable, while at $\omega^{-1} < 25$ d the mountain torque clearly dominates the friction torque T_B .

The coherencies and phases of the cross-spectra between the global AAM M and the torques T_M and T_B in Fig. 2(c) are also instructive. The rather large coherency for both torques in the upper panel of Fig. 2(c) is a sign that the AAM budget is well closed when using the NCEP reanalysis data. The lower panel shows that at nearly all periodicities the mountain torque T_M leads M by almost a quarter of period, hence driving the changes in the latter. This lead-lag quadrature is nearly exact at periodicities $\omega^{-1} < 25$ d, that is when T_M dominates T_B according to Fig. 2(b). The phase of T_B is intermediate between being in opposition and in lead-lag quadrature with M .

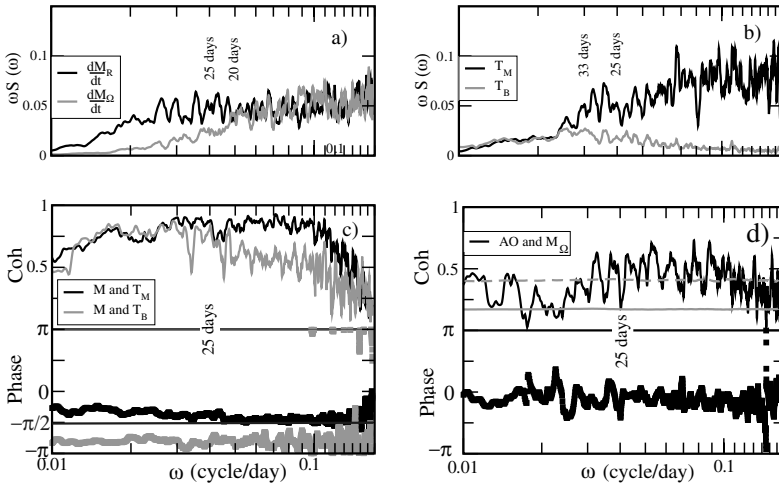


Figure 2. Spectral analysis of different terms in the AAM budget Eqs. (1)–(3). (a) Spectra (S) of the M_R tendency (black solid) and the M_Ω tendency (grey solid). (b) Spectra of T_M (black solid) and T_B (grey solid). (c) Coherency (upper panel) and phase (lower panel) between the global AAM M and (i) T_M (black solid) and (ii) T_B (grey solid). (d) Coherency (upper panel) and phase (lower panel) between the AO and M_Ω . All curves in (a), (b), (c), and (d) are built in 3 steps. First the series are tapered by a 3 d box-car average and sampled every 3 days. Second, their Fourier coefficients are evaluated to produce the periodograms needed for (a) and (b) and the cross-periodograms needed for (c) and (d). The spectra and cross-spectra are then extracted smoothing the (cross-)periodograms by a 30 points (33%) cosine window, yielding a resolution of 6.2×10^{-3} cycles d^{-1} . In (d) a median level (grey solid) and a 1% significance level (grey dashed) have also been added. They are evaluated by a Monte Carlo procedure that applies the cross-spectral analysis to 100 pairs of red-noise uncorrelated series whose variance and lag-one correlation fit the series of northern hemisphere PC 1 and M_Ω both with annual cycle subtracted (see appendix for the extraction of the series with no annual cycle).

On the one hand, the phase opposition implies that large T_B are associated with smaller than usual zonal winds (and hence M_R); on the other hand, the lead-lag quadrature implies that T_B drives M changes through Eq. (1). Thus, T_B has a complex and dual relationship with M , but it remains small compared to T_M (Fig. 2(b)).

The importance of this frequency band for the links between the mass AAM and the AO is proved in Fig. 2(d) which shows a cross-spectral analysis between M_Ω and the AO index. The coherency between the two series is often above 0.5 for $\omega^{-1} < 25$ d while significantly below that value for $\omega^{-1} > 30$ d. For all periodicities the series are nearly in phase (lower panel in Fig. 2(d)). It is also important to emphasize that the coherency values for $\omega^{-1} < 30$ d are nearly always significant at the 1% level and rarely significant for periodicities between 30 and 100 d. The coherency values are also largely above the median value of 0.17 to be expected for uncorrelated series when using our conventional spectral analysis method (see Fig. 2 caption).

Note also that the same analysis applied to M_R and the AO index almost never give significant coherencies for periodicities below 100 d (not shown).

As noted in the introduction and from the literature on this topic, none of the results presented in Figs. 2(a)–(d) are really novel. Nevertheless, they illustrate the specificity of the 1–25 d band, on which we will concentrate in the rest of the paper. To summarize, in this band: M changes are little damped and predominantly driven by the mountain torque; M changes are almost equally distributed between M_Ω and M_R ; and M_Ω changes are significantly correlated with those in the AO.

TABLE 1. STANDARD DEVIATION OF THE DIFFERENT FILTERED SERIES OF AAMS, TORQUES, AND AO INDEX USED IN THE PAPER

	All year	No annual	$\omega^{-1} < 25$ d
M	275 Hd	92 Hd	45 Hd
M_R	263 Hd	80 Hd	33 Hd
M_Ω	67 Hd	45 Hd	31 Hd
T_M	20 H	19 H	18 H
T_B	10 H	8 H	6 H
AO	67 Hd	59 Hd	47 Hd

Units: Hadleys day, 1 Hd = 8.64×10^{22} kg m²s⁻¹; Hadleys, 1 H = 10^{18} kg m²s⁻². Note that the AO index is expressed in terms of Hd instead of Pa. To do this conversion we first normalize the PC 1 values by their DJF standard deviation. Second, we multiply them by the mass angular momentum M_Ω related to the PC 1 regression pattern in Fig. 1(b) using Eq. (2). See text for further details.

3. AAM BUDGET COMPOSITES KEYED TO 1–25 d SERIES

In this section, we use the fact that all the terms in the AAM budget (Eq. (1)) are linear, and consequently Eq. (1) remains valid when each series of AAM and torques are filtered by a non-recursive high-pass filter. Hence, we build series of AAM and torques with substantial spectral power for periodicities, $\omega^{-1} < 25$ d, and very low power for $\omega^{-1} > 35$ d. In the rest of the paper, we will refer to these series as 25-days series; details on the filter used are in appendix. Their standard deviations are given in Table 1. They are compared with the standard deviations of the corresponding unfiltered series and to those of the corresponding series with annual cycle subtracted (see appendix).

The values given in Table 1 clearly show that the high-pass 25 d filter keeps almost all the standard deviation of the unfiltered mountain torque and reduces by a factor around 2 the standard deviation of the boundary-layer torque T_B . The filter also keeps half the variance of the unfiltered mass angular momentum, but strongly attenuates the standard deviation of the wind angular momentum M_R , which possesses a strong annual cycle. The 25-days series of M_R nevertheless accounts for more than 40% of the standard deviation of the M_R series with annual cycle subtracted. Note as well that the standard deviation of the 25-days M_Ω and 25-days M_R are comparable in amplitude, while the 25-days standard deviation of T_M is 3 times larger than the 25-days standard deviation of T_B .

It is important to emphasize that our 25-days series are never small compared to the unfiltered ones. As Table 1 shows, this is also true for the AO. Finally, it is also important to note that the 25-days series close the AAM budget as well as the raw series do: the correlation between the AAM tendency and total torque both evaluated using 25-days series is above 0.88. It is 0.85 when only the contribution of the mountain torque to the 25-days total torque is taken into account.

(a) AAM budget composites

Figures 3(a)–(e) show composites of T_M , T_B , M_Ω , and M_R that are associated with different 25-days series, each indicated on the right of the panels. In Fig. 3(a), for instance, the composites are built from 25-days series of T_M , T_B , M_Ω and M_R , selected each time the 25-days AAM M exceeds a given positive threshold M_+ or is

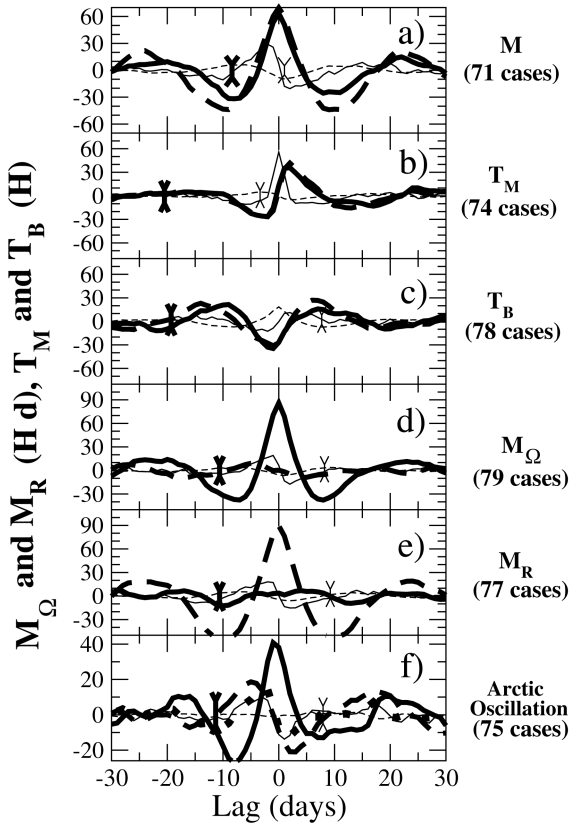


Figure 3. Composites of mountain torque T_M (thin line), boundary-layer torque T_B (thin dashed), mass AAM M_Ω (thick solid), and wind AAM M_R (thick dashed) keyed to 25-days series of: (a) total AAM M , (b) T_M , (c) T_B , (d) M_Ω , (e) M_R , and (f) Arctic Oscillation (northern hemisphere DJF PC 1). The number N of cases used to build the composites are given in parenthesis on the right of each panel. The thin (thick) bar in each panel indicates 1% confidence level from a Monte Carlo test that uses 100 means of T_M (M_Ω), each mean being made with N values of 25-days T_M (M_Ω) taken at random. In (f) the black squares are for the tendency of the M_Ω composite.

below a given negative threshold M_- . At zero lag the T_M composite is the mean of the 25-days T_M values corresponding to the N_+ dates where M exceeds M_+ , minus the mean of the 25-days T_M values corresponding to the N_- dates where M is below M_- . At non-zero lag the composites are built using the same procedure, but with T_M values corresponding to dates at fixed lag from the $N = N_+ + N_-$ local extrema identified before in the 25-days M . The threshold values are arbitrary, and the number N of dates included in a given composite decreases when M_+ (M_-) increases (decreases). We have verified, though, that the composite curves are not very sensitive to moderate changes in the thresholds. The threshold values $M_+ = 115.75$ Hd and $M_- = -124.5$ Hd are used in Fig. 3(a) (units are explained in Table 1). They are about 1.5 times the standard deviation of M with annual cycle subtracted (Table 1). In this case, $N_+ = 36$, $N_- = 35$ so $N = 71$. For the following composites curve (Figs. 3(b)–(e) and later in Figs. 4(a)–(f)) the threshold values for the series to which the 25-days AAM budget is keyed are always chosen to ensure $N_+ \approx N_-$ and $60 < N < 80$, and the value of N is given in parenthesis in all panels. Finally, note that we verified that all composite curves in Figs. 3 and 4 close well, and within the error bound for the mountain torques composite provided, the AAM budget Eqs. (1).

The M_Ω and M_R composites keyed to the 25-days M in Fig. 3(a) present substantial maxima of comparable amplitude at zero lag. ‘Substantial’ means comparable with the standard deviation of the unfiltered M_Ω series given in Table 1. As suggested by the spectral analysis in section 2, this follows from the fact that in the 1–25 d band both M_R and M_Ω make comparable contributions to the global AAM. The black line in Fig. 3(a), shows that the M positive anomaly at zero lag is preceded by a substantial positive mountain torque anomaly (Table 1) that is above 15 H for lags $-7 \text{ d} < l < 0 \text{ d}$, and followed by a subsequent negative mountain torque anomaly that is below -15 H . This composite map thus strongly suggests that the AAM changes in the 1–25 d band are driven by the mountain torque and divided between mass and wind angular momentum. This conclusion is supported by the fact that the composite of the 25-days T_B keyed to the 25-days M (black dashed in Fig. 3(a)) is very small compared to the T_M composite and is in phase opposition with the M_Ω and M_R composites at nearly 0 d lag. This corroborates the cross-spectral results in Fig. 2(c), where in the 1–25 d band the mountain torque drives the M changes.

To support this point even further, Fig. 3(b) presents composites according to the 25-days T_M . The T_M composite presents a substantial spike which lasts less than 5–6 d typically and which maximum value is almost 60 H. It is associated with rather abrupt increases in M_Ω and M_R centred at zero lag, that are almost identical in phase and amplitude.

To support the hypothesis that the boundary-layer torque damps the AAM anomalies, we also made composites along the 25-days T_B (Fig. 3(c)). The M_Ω and M_R composites are nearly in phase with each other but almost in phase opposition with the composite in T_B . Also in this case the composite of the mountain torque seems to remain the driver (Fig. 3(c)).

Figure 3(d), tests what can cause changes in M_Ω only: again the mountain torque (black solid) is the driver. Conversely, Fig. 3(e) tests what can cause changes in M_R only, giving very similar conclusions: the mountain torque again.

Finally, Fig. 3(f) presents composites keyed to the 25-days AO. At zero and small negative lag the AO is associated with a substantial positive anomaly in M_Ω whose maximum is at $l = -1 \text{ d}$. It is preceded by an extrema in T_M close to 9 H at $l = -3 \text{ d}$ lag and followed by a minimum in T_M close to -14 H at $l = 1 \text{ d}$ lag. Since these extrema in T_M are significant (black arrow) and quite substantial (Table 1), the maximum in M_Ω is likely to be largely driven by the mountain torque. This point is confirmed by the fact that the tendency of the M_Ω composite (black squares in Fig. 3(f)) is very near the composite in T_M . The only fact that can complicate this interpretation is that M_R varies quite substantially during the 25-days cycle of the AO shown in Fig. 3(f). The changes in M_R at negative lag $10 \text{ d} < l < 0 \text{ d}$ seem in opposition with those in M_Ω , suggesting that there are torque-free exchanges between M_R and M_Ω during the AO cycle. Nevertheless, we verified that these changes in M_R have moderate impacts on the global composite M tendency which stays very near the black squares in Fig. 3(f). It thus remains true that the AAM anomalies associated with the AO are essentially due to changes in M_Ω , which are themselves driven by the mountain torque.

(b) Mountain torques evaluated over different latitude bands

As noted in section 1, the fact that the AAM response to mountain torques is equally distributed between mass and wind angular momentum can simply result from the geostrophic balance and from the fact that the major mountain ranges are located in the midlatitudes. If such an explanation is relevant to the real atmosphere, the balance between M_Ω and M_R must vary when the central latitude θ_0 of the mountain ranges that

produce the torque varies, simply because the Coriolis parameter varies in $\sin \theta_0$ and because the distance to the rotation axis varies in $\cos \theta_0$.

To check if this is the case, we evaluate the contribution of six different non-overlapping latitudinal sectors to the mountain torque. For this, we limit the T_M integration in Eq. (3) to the latitude band of interest. Among the sectors selected, two cover the polar regions, the Arctic (60°N – 90°N) and the Antarctic (60°S – 90°S), one covers the equatorial band (15°S – 15°N) and three cover the midlatitude and subtropical latitudes, one the southern hemisphere (15°S – 60°S), one the subtropical northern hemisphere (15°N – 35°N), and one the midlatitude northern hemisphere (35°N – 60°N). The choice of these different latitude bands is somewhat arbitrary. It is motivated by the fact that the latitudinal bands need to be sufficiently large to provide substantial contributions to the mountain torque. For instance, this constraint means that we have grouped together the subtropical and midlatitudes southern hemisphere: at these time-scales the Andes make a rather small contribution to T_M compared to the Rockies and the Himalayas. On the other hand, because the mountain ranges in the northern hemisphere are very large, we can distinguish in the northern hemisphere the subtropical and the midlatitude regions.

Once these series of torque have been built, they are again filtered in the 1–25 d band and composites of the AAM budget are constructed according to each of them. The composites according to the 25-days T_M in the Arctic region are displayed in Fig. 4(a). The global 25-days T_M composite presents a significant spike that peaks at 20 H at zero lag, and that lasts around 3 d. It is largely due to Greenland (not shown), and the sectorial torque almost identifies with the total mountain torque. In correspondence with this spike the mass angular momentum composite varies substantially from below -14 Hd to 9 Hd, while the wind angular momentum varies comparatively less. Away from this 3 d lag window, none of the values of torque and AAM are significant (black and grey arrows in Fig. 4(a)).

A rather comparable behaviour can be seen when the contribution of Antarctica to the torque is considered (Fig. 4(f)). It is important to note that in both Figs. 4(a) and (f) the extrema of mass AAM obtained at small negative and positive lags are only marginally significant. Although this can reduce the explanatory power of our interpretation, one remark can be made. The change of M_Ω from a significant negative value at small negative lag to a significant positive one at small positive lag (Figs. 4(a)–(f)) indicates rather strong tendencies (not shown) which are far more significant than the anomalies of M_Ω themselves.

If we now turn to the contribution of the equatorial band to the mountain torque in Fig. 4(d), we find a behaviour that is nearly opposite to that found in the polar regions: a lag-zero peak close to 15 H in T_M lasting nearly 6 d, corresponds within the same period to an abrupt and significant increase in the wind AAM M_R , while the mass AAM M_Ω varies moderately during the same interval. Note, nevertheless, that in this case the sectorial torque is significantly smaller than the total torque indicating contributions from extratropical latitudes to the results in Fig. 4(d) that may explain the changes in M_Ω .

When we look at the midlatitude and subtropical sectors (Figs. 4(b), (c) and (e)), significant peaks in mountain torques lasting a few days are associated with subsequent increased M_R and M_Ω . For all these three sectors the increases in M_Ω compare, within error bounds, in phase and amplitude with those in M_R . Again, some small but significant discrepancies between sectorial mountain torques and global mountain torques are present in Figs. 4(b) and (c). These indicate the limit of our approach, because the major mountain ranges are not necessarily well embedded within the latitudinal sectors that we chose.

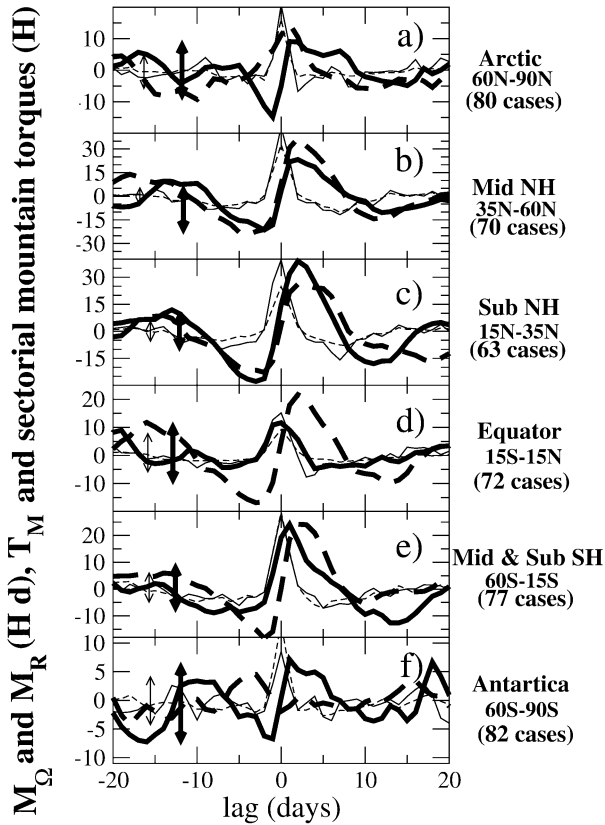


Figure 4. Composites of the 25-days AAM budget, keyed to 25-days mountain torques evaluated over six different non-overlapping latitude sectors. The sector and the number of cases taken to build the composites are given on the right of each panel. Same conventions and parameters as in Fig. 3 except that the thin dashed lines are for the composite of the sectorial mountain torques.

When comparing the amplitude of the T_M composites in each panel of Fig. 4, it is clear that the subtropical and midlatitudes make the largest contributions to the mountain torque. This explains why the same balance holds for the global mountain torque anomalies in Fig. 3(b) since the subtropics and midlatitudes induce changes in M where $M_R \approx M_\Omega$.

4. SHALLOW-WATER MODEL FOR THE PARTITION BETWEEN M_Ω AND M_R

In this part, we present results in a very simple dynamical context to understand more precisely the partition between mass AAM and wind AAM. We study the zonal mean-flow response to a body force acting on a zonally symmetric shallow-water flow on a sphere. We furthermore assume that this body force is not modulated by the axisymmetric flow, which excludes that it can be due to frictional effects. This force only mimics mountain torques, the latter being due to circulation patterns that are not axisymmetric, within a good approximation (see Lott *et al.* 2004, Fig. 2). Accordingly, our model is only adapted to interpret the actual AAM budget for situations where the boundary-layer torque plays a minor role, which is the case for the 25-days series used

in section 3. The set of equations used are similar to Gill (1982, p. 431):

$$\left(\frac{\partial}{\partial t} + \frac{v}{r} \frac{\partial}{\partial \theta} \right) u - \left(2\Omega + \frac{u}{r \cos \theta} \right) v \sin \theta = \frac{F}{h}, \quad (4)$$

$$\left(\frac{\partial}{\partial t} + \frac{v}{r} \frac{\partial}{\partial \theta} \right) v + \left(2\Omega + \frac{u}{r \cos \theta} \right) u \sin \theta = -\frac{g}{r} \frac{\partial h}{\partial \theta}, \quad (5)$$

$$\frac{\partial h}{\partial t} + \frac{1}{r \cos \theta} \frac{\partial h v \cos \theta}{\partial \theta} = 0. \quad (6)$$

In Eqs. (4)–(6), u , v and h are the zonal wind, the meridional wind and the fluid depth, respectively; g is the gravity constant; F is a body force that varies in time and latitude. Linearized around a state of rest with constant depth H_0 , the Eqs. (4)–(6) correspond to the Laplace tidal equation for zonal wave number zero (Longuet-Higgins 1968).

The set of Eqs. (4)–(6) satisfies an AAM budget of the form

$$\frac{d}{dt} (M_R + M_\Omega) = T_F, \quad (7)$$

where the wind AAM, the mass AAM, and the torque due to F are

$$\left. \begin{aligned} M_R &= 2\pi r^3 \int_{-\pi/2}^{+\pi/2} hu \cos^2 \theta \, d\theta, \\ M_\Omega &= 2\pi r^4 \Omega \int_{-\pi/2}^{+\pi/2} (h - H_0) \cos^3 \theta \, d\theta, \end{aligned} \right\} \quad (8)$$

$$T_F = 2\pi r^3 \int_{-\pi/2}^{+\pi/2} \cos^2 \theta F \, d\theta. \quad (9)$$

(a) Approximate analytical solutions

The fact that the wind AAM and the mass AAM are linked via the geostrophic balance can be illustrated by two approximate solutions of the set of Eqs. (4)–(6). In the first, the atmosphere response to the force F after its end is assumed to be a uniform constant zonal wind U that is equilibrated by a surface elevation,

$$H = H_0 + \frac{rU\Omega}{g} \left(2 \cos \theta - \frac{\pi}{2} \right), \quad (10)$$

through the Coriolis force

$$2\Omega \sin \theta U = -\frac{g}{r} \frac{\partial H}{\partial \theta}. \quad (11)$$

The solution in Eq. (10) is such that H and H_0 correspond to the same total mass. For this solution, and using Eqs. (8), the fraction between mass AAM and wind AAM is

$$\frac{M_\Omega}{M_R} = \frac{r^2 \Omega^2}{6gH_0}, \quad (12)$$

For parameters representative of the earth troposphere, $g = 9.81 \text{ m s}^{-2}$, $H_0 = 8 \text{ km}$, $r = 6400 \text{ km}$ and $\Omega = 7.27 \times 10^{-5} \text{ s}^{-1}$ this ratio is near 0.45. Equation (12) predicts well that geostrophy implies that M must be proportionately distributed between M_Ω and M_R but the fraction M_Ω/M_R is underestimated by a factor around 2 compared to

the equipartition found in Figs. 3(a) and (b). We attribute this mismatch to the fact that the major mountain ranges are located off the equator, inducing changes in 25 d winds that are not uniform over the entire atmosphere.

In a second approximate solution, we try to account for this geographical effect and assume that the force F applies to the flow within a very thin latitude band with width $\delta\theta \ll 1$ centred at a latitude θ_0 . Assuming that, after the force ends, the wind response U is constant in this band and null elsewhere, that the height response H equilibrates U in this band via the Coriolis force and is constant elsewhere and that H and H_0 correspond to the same total mass, the fraction between mass AAM and wind AAM is given by

$$\frac{M_\Omega}{M_R} = \frac{r^2\Omega^2}{gH_0} \frac{2}{3} \sin^2 \theta_0. \quad (13)$$

This ratio is null at the equator, approximately equal to 1.84 at the poles and to 0.95 when $\theta_0 = \pm 45^\circ$. This expression thus recovers at least qualitatively the latitudinal dependence between M_R and M_Ω found in the observations in Fig. 4.

(b) Numerical time-dependent model

Although relevant for our study, the approximate ratios in Eqs. (12)–(13) rely on assumptions about the spatio-temporal structure of U and H that are highly idealized. Furthermore they do not allow us to describe the transient dynamics underlying the redistribution between mass and momentum that leads to such ratios. To evaluate these ratios in a more complete dynamical context, and for different forcings F , we solve the set of Eqs. (4)–(6) with a finite-difference model that uses the transformed latitude coordinate $\mu = \sin \theta$ and the set of variables h , $hu \cos \theta$ and $hv \cos \theta$. In this coordinate system the model grid is staggered, with h evaluated at $M + 1$ grid points that are equally spaced and that include both poles, while $hu \cos \theta$ and $hv \cos \theta$ are evaluated at the M grid points centred between the h -grid points. In all the experiment presented, $M = 1000$ points is used, a value for which convergence is achieved and the AAM budget (Eq. (7)) is perfectly closed. In space, all the differentiations in Eqs. (4)–(6) are estimated with centred finite differences. In time, the integration is made by successive explicit leapfrog steps followed by an Asselin filter (Haltiner and Williams 1976).

Except when specified, all the experiments presented last 30 d and have a time step $dt = 10$ s. The forcing F is always centred on a latitude θ_0 and covers a latitude band of width $\delta\theta = 10^\circ$. In time, it starts from 0 at $t = 0$, reaches a maximum amplitude at $t = \tau_F$ and returns to zero at $t = 2\tau_F$. Accordingly, it is null at all times for $\theta > \theta_0 + \delta\theta/2$ and $\theta < \theta_0 - \delta\theta/2$, and it is null everywhere for $t > 2\tau_F$. For $\theta_0 - \delta\theta/2 < \theta < \theta_0 + \delta\theta/2$ and $0 < t < 2\tau_F$ it is given by

$$F = F_0 \frac{4}{\delta\theta^2} \left(\theta - \theta_0 + \frac{\delta\theta}{2} \right) \left(\theta_0 + \frac{\delta\theta}{2} - \theta \right) \left\{ 1 - \cos^2 \left(\frac{\pi t}{2\tau_F} \right) \right\}. \quad (14)$$

In all experiments the value of F_0 is taken so that the maximum of the torque reaches $T_F(\tau_F) = 10$ H. In most experiments, we will also take the forcing time-scale $\tau_F = 2.5$ d, a value which ensures that the time-scale of the response is large compared to that of the planetary gravity modes. In non-dimensional form this condition becomes

$$(\Omega\tau_F)^2 = 225 \ll \frac{r\Omega}{\sqrt{gH_0}} = 1.66. \quad (15)$$

For this value of τ_F we can expect that the response of the rotational modes far exceeds the gravity modes, i.e. the situation is adjusted.

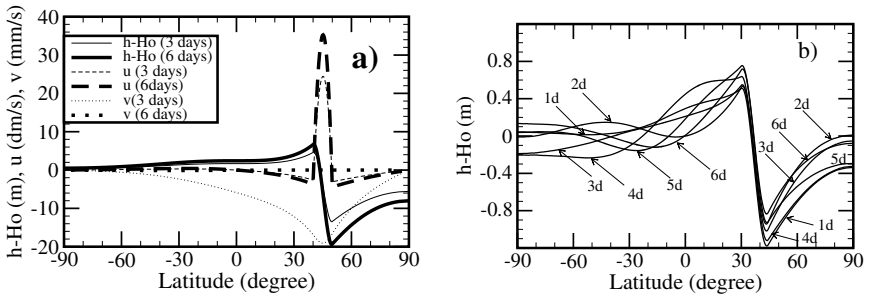


Figure 5. Shallow-water model results, forcing F centred at $\theta_0 = 45^\circ\text{N}$. (a) Slowly varying case $2\tau_F = 5$ d: Flow profiles of $h - H_0$ (solid) u (dashed), and v (dot) at $t = 3$ d (thick) and $t = 6$ d (thin). (b) Rapidly varying case $2\tau_F = 12$ hours: $h - H_0$ every day. See text for further explanation.

Nevertheless, and for completeness, we will discuss as well the response when F varies rapidly and take in one case $\tau_F = 0.25$ d. In this case

$$(\Omega\tau_F)^2 = 2.8 \approx r\Omega / \sqrt{gH_0} = 1.66,$$

a situation that sometimes occurs in GCMs if not in reality, and in response to gravity-waves parametrizations (Egger 2003).

(c) Results

Figure. 5(a) shows the flow response in the slowly varying case $\tau_F = 2.5$ d, and when the forcing F is centred at the latitude $\theta_0 = 45^\circ\text{N}$. The response in Fig. 5(a) is shown at two different instants, one chosen when the force F is non-zero ($t = 3$ d) and one after the force has stopped ($t = 6$ d). At $t = 3$ d, the positive force F essentially produces a meridional ageostrophic negative velocity v that presents a minimum near θ_0 where it does equilibrate F via the Coriolis force. This southward velocity is associated with a southward flux of mass whose minimum is near θ_0 as well. Accordingly, the surface elevation increases to the south of θ_0 and decreases to the north of it. In geostrophic equilibrium with h , the zonal wind presents a pronounced positive zonal jet u in the area where F is non-zero and where the elevation h shows a strong negative gradient (between $\theta_0 - \delta\theta/2 = 40^\circ\text{N}$ and $\theta_0 + \delta\theta/2 = 50^\circ\text{N}$). Away from that area the gradient of h is everywhere positive and by geostrophy u is negative in the northern hemisphere and positive in the southern hemisphere. Note that the final profiles of h and u differ substantially from the idealized case considered in Eq. (13), which assume constant height and zero velocity at all locations apart from the narrow latitude band $\theta_0 - \delta\theta/2 < \theta < \theta_0 + \delta\theta/2$.

Such a balanced description of the flow evolution remains valid as long as F is non-zero, and the force keeps deepening the trough in h north of θ_0 and raising the high south of it. Hence the zonal flow u keeps increasing in amplitude around θ_0 . For $t > 2\tau_F$, $F = 0$ and the ageostrophic velocity it induces, $v = 0$, as well (Fig. 5(a)). At this time the profiles of h and u no longer evolve, and they keep the values they reached at $t = 2\tau_F$ (see also Fig. 5(a)).

The fact that the flow no longer evolves after the forcing ends reflects the fact that the dynamics is essentially linear and balanced. Indeed, for all the waves that could exist after the forcing ends, the dispersion relationship of the balanced ones degenerate into $\omega = 0$ (for a rigorous derivation of the rotational modes in the context of tides with zonal wave number 0 see Tanaka and Kasahara (1992); but this is classic behaviour, see for instance the $k = 0$ axis of the tropical wave dispersion relationship given in Gill 1982).

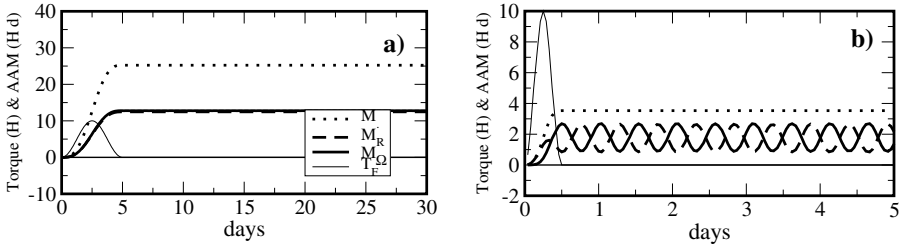


Figure 6. AAM and torque evolutions in the shallow-water model, forcing F centred at $\theta_0 = 37.5^\circ\text{N}$: (a) Slowly varying case $2\tau_F = 5$ d, (b) Rapidly varying case $2\tau_F = 12$ hours. M (dotted), M_Ω (thick solid), M_R (dashed), and T_F (thin solid). See text for explanation of symbols.

In contrast, when the forcing varies rapidly ($\tau_F = 6$ hours, Fig. 5(b)) the response never reaches a steady state and some of the gravest gravity modes are substantially excited. After the forcing ends, they induce planetary-scale oscillations (Fig 5(b)) that modulate the surface elevation around the steady response depicted in Fig. 5(a).

(d) Angular momentum budget

The evolution of the angular momentum in the slowly varying and in the rapidly varying cases described above are presented in Figs. 6(a) and (b), respectively. In both cases the torque T_F reaches a maximum value of 10 H at $t = \tau_F$ and induces an increase in total AAM M that lasts $2\tau_F$. After the torque returns to 0 ($t > 2\tau_F$) M stays constant. In the slowly varying case (Fig. 6(a)), and at all times during the simulation, M is equally distributed between M_Ω and M_R . In this case, the change in distribution of mass seen in the profile of h (Fig. 5(a)) is associated with an increase in M_Ω that equals the increase in M_R associated with the zonal wind u (Fig. 5(a)) in geostrophic balance with h .

When the force varies rapidly, the partition between M_R and M_Ω never reaches a constant value (Fig. 6(b)). At the very beginning for instance, the force varies so fast that it induces a zonal-wind acceleration instead of being equilibrated by a meridional velocity via the Coriolis force and M_R increases first (Fig. 6(b)). Rapidly, and within a time-scale that compares with the inertial oscillation periodicity, M_Ω starts to increase as well to become twice as big as M_R at $t = 2\tau_F = 12$ h. Thereafter, the presence of gravity-wave modes in the system makes both M_Ω and M_R oscillate with a periodicity which in that case is slightly below 1 d. For both M_R and M_Ω these oscillations take place around a mean value that is close to $M/2$ and have an amplitude that approaches as well $M/2$.

Since the dataset derived from the NCEP/NCAR reanalysis cannot properly sample oscillations with periods close to 1 d, we will focus next on sensitivity tests to the forcing location rather than duration. We assume that the balance dynamics at work in Fig. 5(a) are good enough in reality to explain our composite results in section 3, so we take $2\tau_F = 5$ d.

Figure 7(a) presents the ten profiles of F that have been used to test the sensitivity of our results to the latitude. Figure 7(b) presents the final values of M_R and M_Ω corresponding to these ten forcings. First, in all ten experiments, the final value of the AAM is $M_R + M_\Omega = 25$ Hd, which follows that T_F is not changed from one experiment to the other. Second, the latitudinal dependence on the forcing found in the dataset in section 3 is well reproduced by the model. In particular, when the forcing is centred at the equator ($\theta_0 = 0$) it only induces a zonal-wind acceleration as the Coriolis force is very small and the AAM is almost entirely due to M_R .

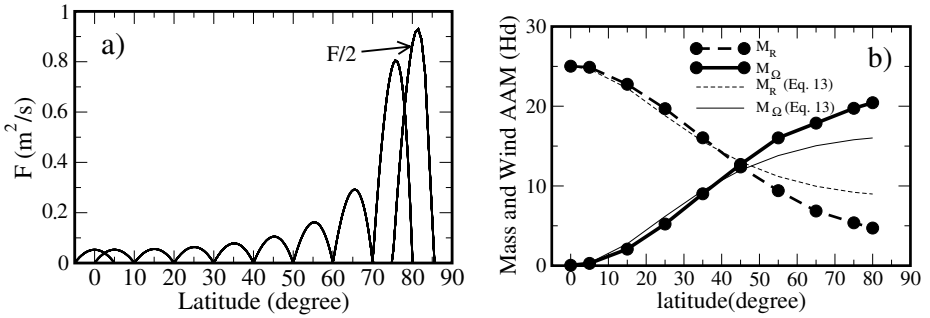


Figure 7. Sensitivity of the shallow-water model response to the central latitude θ_0 of the forcing F . (a) 10 Profiles of F used. (b) Final model values of M_Ω (thick solid with dots) and M_R (thick dashed with dots); theoretical values deduced from Eq. (13) are in thin solid (M_Ω) and thin dashed (M_R). See text for explanation of symbols.

As the forcing moves off the equator, it induces meridional ageostrophic circulations whose importance increases as a function of latitude. As this meridional circulation directly affects the surface elevation, the importance of M_Ω compared to that of M_R in the budget of M increases. When the force is centred at midlatitudes, M_Ω and M_R are approximately equal. When F is centred at northern and polar latitudes, M_Ω exceeds M_R substantially.

The results in Fig. 7 compare also rather well with the theoretical result in Eq. (13), at least in the Tropics and in the midlatitudes. The skill of Eq. (13) nevertheless degrades north of 45°N . At 80°N , for instance, the ratio $M_\Omega/M_R \approx 4.4$ in the numerical simulations while Eq. (13) gives $M_\Omega/M_R \approx 1.8$.

For completeness, we have also made sensitivity tests of the results in Fig. 7 to the model parameters g and H_0 . When those parameters vary, the qualitative behaviour of Fig. 7 remains the same. The importance of M_Ω increases as the forcing moves towards the pole. The central latitude for which $M_\Omega \approx M_R$ is nevertheless quite sensible to these two parameters: it moves towards the pole as $\sqrt{gH_0}$ increases. This behaviour is also predicted by Eq. (13).

5. CONCLUSION

(a) Summary

This study seeks to identify the relative importance of wind AAM M_R versus mass AAM M_Ω in the high-frequency ($\omega^{-1} \leq 25$ d) fluctuations of global AAM M , identify the dynamical origin of this balance, and isolate one mechanism that drives high-frequency fluctuations in the Arctic Oscillation. We find that the mountain torque T_M is producing the AAM fluctuations, the friction torque T_B being much smaller and essentially damping them. Composite anomalies of the AAM budget keyed to the 25 d T_M reveal that the characteristic M response to mountain torques is equally distributed between M_Ω and M_R . We interpret this result as a signature of the balanced dynamics affecting the atmospheric response to mountain torque anomalies at periodicities above 1 d.

To corroborate this interpretation we present composite anomalies of the AAM budget keyed to mountain torques evaluated over different latitudinal sectors (hence changing the Coriolis force). For T_M anomalies produced in the polar regions, the

response in M_Ω exceeds that in M_R while it is the other way around when the mountain torque is produced in the Tropics. When T_M is produced in the subtropics and in the midlatitudes the response in M is equally distributed between M_R and M_Ω . Since these sectors also contain the major mountain ranges, this explains why the same balance holds for the global mountain torque. The dependence on the latitude of the forcing is the first confirmation that the geostrophic balance controls the distribution of M between M_R and M_Ω , as expected from simple theoretical considerations.

Further evidence is provided by a one-layer shallow-water model for zonal flow on a rotating sphere. In this model, positive forces lasting a finite amount of time and centred at different latitudes are specified and the adjustment of the system to these forces is analysed. When the forcing varies sufficiently slowly so that the response is devoid of large-scale gravity modes, the model reproduces qualitatively the observational results. In particular, $M_R \approx M_\Omega$ when the force is centred around 45°N , while $M_R \rightarrow 0$ when the force is moved towards the poles, and $M_\Omega \rightarrow 0$ when the force is moved towards the equator. When the forcing varies sufficiently fast so that large-scale gravity modes are excited, steady values for M_R and M_Ω are never obtained. M_R and M_Ω present substantial oscillations but their time-mean values retains the ratio predicted in the slowly varying context.

(b) Bearings on the AO

The fact that the AO can be affected during the exchanges of momentum between the solid earth and the atmosphere that occur in the polar and midlatitude is quite an interesting result in itself. This is due to the fact that the AO pattern is associated with substantial mass AAM, as it corresponds to a redistribution of mass from the polar latitude to the midlatitudes. This suggests that the mountain torque could be used as one of the predictors of its changes as already found by Lott *et al.* (2004) in the 20–30 d band. On top of the spectral coherency between the AO and M_Ω given in Fig. 2(d), more quantitative arguments to support this finding are also given here. One of them is little discussed in the text but is implicit in Table 1, where the AO standard deviation is expressed in Hd. The conversion is done by using the surface pressure map regressed onto the DJF PC 1 (Fig. 1(b)) into the mass angular momentum (Eq. (2)). In amplitude, the AO standard deviation compares well with that of M_Ω (Table 1) which means that mountain torques are large enough to drive AO changes, at least in part. This is of course confirmed by the composites of the AAM budget keyed to the 25-days AO in Fig. 3(f): they present substantial variations in M_Ω driven in good part by the mountain torque T_M . Another argument refers to the model in section 4: if we transform the surface elevation in the model into surface pressure, the variations of 20 m due to a 10 H torque that lasts 5 d (seen in Fig. 5) correspond to surface pressure variations close to 2 hPa. For torque values close to 50 H (consistent with the values of the composites in Figs. 3–4), the surface pressure signature can easily reach more than 10 hPa. This value is close to the largest pressure difference in the AO regression map in Fig. 1(b).

These findings can be useful in the context of mountains representation in GCMs (Lott 1999; Webster *et al.* 2003). As mountains affect substantially at least one of the dominant modes of atmospheric variability, it is clear that the way they are taken into account should be tested against the AAM budget issued from reanalysis data. In this context, it is noteworthy that the subgrid-scale orographic representation scheme that has been validated at best against field data (Lott and Miller 1997) should also be validated globally, and designed to improve the spectra of the different term of the AAM budget, at least at periodicities $\omega^{-1} < 25$ d.

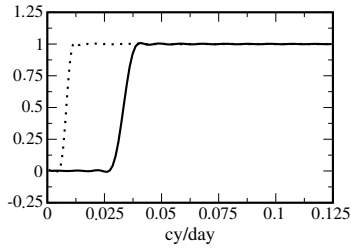


Figure A.1. Transfer functions of the two filters used to build the 25-days series (solid) and the series without annual cycle (dashed).

APPENDIX

Filtered series

To focus on the 1–25 d band revealed by the spectral analysis in section 2, a high-pass non-recursive filter is applied to the AAM budget series. This filter uses a Kaiser window with parameters adjusted to minimize Gibbs effects (Hamming 1983; Scavuzzo *et al.* 1998). Its transfer function (Fig. A.1) has its half-power point at $\omega^{-1} = 30$ d, is close to zero at periodicities $\omega^{-1} > 40$ d, and is close to one for $\omega^{-1} < 25$ d. Also note that we applied a comparable filter with half-power point at 120 d to the series when needed (essentially in Table 1). This filter attenuates strongly the annual and semi-annual cycles: its transfer function (Fig. A.1) is close to zero, for $\omega^{-1} > 180$ d and close to one for $\omega^{-1} < 90$ d.

ACKNOWLEDGEMENTS

We are grateful to the three referees for their helpful comments. In particular, we are grateful to Dr Joseph Egger (Referee A) for suggesting the analytical formula in Eq. (12) and to Dr Steven Marcus (Referee C) for suggesting that in Eq. (13).

REFERENCES

- | | | |
|---|------|--|
| Chao, B. F. | 1984 | Interannual length-of-day variation with relation to the Southern Oscillation/El Niño. <i>Geophys. Res. Lett.</i> , 11 , 541–544 |
| Dickey, J. O., Ghil, M. and Marcus, S. L. | 1991 | Extratropical aspects of the 40–50 day oscillation in length-of-day and atmospheric angular momentum. <i>J. Geophys. Res.</i> , 96 , 22643–22658 |
| Egger, J. | 2003 | Gravity wave drag and global angular momentum: geostrophic adjustment processes. <i>Tellus</i> , 55A , 419–425 |
| Gill, A. E. | 1982 | <i>Atmosphere–Ocean dynamics</i> . International Geophysics Series, Academic Press, New York |
| Haltiner, R. and Williams, T. | 1976 | <i>Numerical prediction and dynamic meteorology</i> , 2nd edition. Wiley |
| Hamming, R. W. | 1983 | <i>Digital filters</i> . Prentice-Hall |
| Hendon, H. H. | 1995 | Length of day changes associated with the Madden–Julian Oscillation. <i>J. Atmos. Sci.</i> , 52 , 2373–2383 |
| Huang, H. P., Sardeshmukh, P. D. and Weickmann, K. M. | 1999 | The balance of global angular momentum in a long-term atmospheric data set. <i>J. Geophys. Res.</i> , 104 , 2031–2040 |
| Iskenderian, H. and Salstein, D. A. | 1998 | Regional sources of mountain torque variability and high frequency fluctuations in atmospheric angular momentum. <i>Mon. Weather Rev.</i> , 126 , 1681–1694 |
| Kang, I. S. and Lau, K. M. | 1994 | Principal modes of atmospheric circulation anomalies associated with global angular momentum fluctuations. <i>J. Atmos. Sci.</i> , 51 , 1194–1205 |

- Kalnay, E., Kanamitsu, M., Kistler, R., Collins, W., Deaven, D., Gandin, L., Iredell, M., Saha, S., White, G., Woollen, J., Zhu, Y., Leetmaa, A., Reynolds, R., Chelliah, M., Ebisuzaki, W., Higgins, W., Janowiak, J., Mo, K. C., Ropelewski, C., Wang, J., Jenne, R. and Joseph, D. 1996 The NCEP/NCAR 40-year reanalysis project. *Bull. Am. Meteorol. Soc.*, **77**, 437–472
- Lejenäs, H. and Madden, R. A. 2000 Mountain torques caused by normal-mode global Rossby waves, and the impact on atmospheric angular momentum. *J. Atmos. Sci.*, **57**, 1045–1051
- Longuet-Higgins, M. S. 1968 The eigenfunctions of Laplace tidal equations over a sphere. *Phil. Trans. R. Soc. London*, **A262**, 511–607
- Lott, F. 1999 Alleviation of stationary biases in a GCM through a mountain drag parametrization scheme and a simple representation of mountain lift forces. *Mon. Weather Rev.*, **127**, 788–801
- Lott, F. and Miller, M. 1997 A new sub-gridscale orographic drag parameterization; its testing in the ECMWF model. *Q. J. R. Meteorol. Soc.*, **123**, 101–127
- Lott, F., Robertson, A. W. and Ghil, M. 2001 Mountain torques and atmospheric oscillations. *Geophys. Res. Lett.*, **28**, 1207–1210
- 2004 Mountain torques and northern-hemisphere low-frequency variability Part I: Hemispheric aspects. *J. Atmos. Sci.*, **61**, 1259–1271
- Madden, R. A. 1987 Relationship between changes in the length of day and the 40 to 50-day oscillation in the tropics. *J. Geophys. Res.*, **92**, 8391–8399
- Newtown, C. W. 1971 Mountain torques in the global angular momentum balance. *J. Atmos. Sci.*, **28**, 623–628
- Preisendorfer, R. W. 1988 *Principal component analysis in meteorology and oceanography*. Elsevier, New York
- Rosen, R. D. 1993 The axial momentum balance of Earth and its fluid envelope. *Surv. Geophys.*, **14**, 1–29
- Rosen, R. D. and Salstein, D. A. 1983 Variations in atmospheric angular momentum on global and regional scales and the length of day. *J. Geophys. Res.*, **88**, 5451–5470
- Scavuzzo, C. M., Lamfri, M. A., Teitelbaum, H. and Lott, F. 1998 A study of the low frequency inertio-gravity waves observed during PYREX. *J. Geophys. Res.*, **103**, 1747–1758
- Starr, V. P. 1948 An essay on the general circulation of the earth's atmosphere. *J. Meteorol.*, **5**, 39–43
- Swinbank, R. 1985 The global atmospheric angular momentum balance inferred from analyses made during the FGGE. *Q. J. R. Meteorol. Soc.*, **111**, 977–992
- Tanaka, H. L. and Kasahara, A. 1992 On the normal modes of Laplace tidal equations for zonal wave number zero. *Tellus*, **44a**, 18–32
- Thompson, D. W. and Wallace, J. M. 1998 The Arctic Oscillation signature in the wintertime geopotential height and temperature fields. *Geophys. Res. Lett.*, **25**, 1297–1300
- von Storch, J.-S. 1994 Interdecadal variability in a global coupled model. *Tellus*, **46A**, 419–432
- 1999 The reddest atmospheric modes and the forcing of the spectra of these modes. *J. Atmos. Sci.*, **56**, 1614–1626
- von Storch, H. and Zwiers, F. W. 1999 *Statistical analysis in climate research*. Cambridge University Press
- Wallace, J. M. 2000 North Atlantic Oscillation/annular mode: Two paradigms—one phenomenon. *Q. J. R. Meteorol. Soc.*, **126**, 791–806
- Webster, S., Brown, A. R., Cameron D. R. and Jones, C. P. 2003 Improvements of the representation of orography in the Met Office Unified Model. *Q. J. R. Meteorol. Soc.*, **129**, 1989–2010
- Weickmann, K. M. and Sardeshmuckh, P. D. 1994 The atmospheric momentum budget cycle associated with a Madden-Julian Oscillation. *J. Atmos. Sci.*, **51**, 3194–3208
- Weickmann, K. M., Kiladis, G. N. and Sardeshmuckh, P. D. 1997 The dynamics of intraseasonal atmospheric angular momentum oscillations. *J. Atmos. Sci.*, **54**, 1445–1461
- Wolf, W. L. and Smith, R. B. 1987 Length-of-day changes and mountain torque during El-Niño. *J. Atmos. Sci.*, **44**, 3656–3660